

Sailable Direct Covariance Wind Stress in Various Wind and Current Regimes of the Tropical Pacific

J. E. JACK REEVES EYRE^{a,b}, MEGHAN F. CRONIN^b, DONGXIAO ZHANG,^{a,b} ELIZABETH J. THOMPSON,^c CHRISTOPHER W. FAIRALL,^c AND JAMES B. EDSON^d

^a *Cooperative Institute for Climate, Ocean and Ecosystem Studies, University of Washington, Seattle, Washington*

^b *NOAA/Pacific Marine Environmental Laboratory, Seattle, Washington*

^c *NOAA/Physical Sciences Laboratory, Boulder, Colorado*

^d *Woods Hole Oceanographic Institution, Woods Hole, Massachusetts*

(Manuscript received 21 July 2022, in final form 24 January 2023, accepted 16 February 2023)

ABSTRACT: High-frequency wind measurements from Sailable autonomous surface vehicles are used to calculate wind stress in the tropical east Pacific. Comparison between direct covariance (DC) and bulk wind stress estimates demonstrates very good agreement. Building on previous work that showed the bulk input data were reliable, our results lend credibility to the DC estimates. Wind flow distortion by Sailables is comparable to or smaller than other platforms. Motion correction results in realistic wind spectra, albeit with signatures of swell-coherent wind fluctuations that may be unrealistically strong. Fractional differences between DC and bulk wind stress magnitude are largest at wind speeds below 4 m s^{-1} . The size of this effect, however, depends on choice of stress direction assumptions. Past work has shown the importance of using current-relative (instead of Earth-relative) winds to achieve accurate wind stress magnitude. We show that it is also important for wind stress direction.

SIGNIFICANCE STATEMENT: We use data from Sailable uncrewed oceanographic research vehicles to investigate the horizontal forces applied to the surface of the ocean by the action of the wind. We compare two methods to calculate the forces: one uses several simplifying assumptions, and the other makes fewer assumptions but is error prone if the data are incorrectly processed. The two methods agree well, suggesting that Sailable vehicles are suitable for both methods and that the data processing methods work. Our results show that it is important to consider ocean currents, as well as winds, in order to achieve accurate magnitude and direction of the surface forces.


KEYWORDS: Atmosphere-ocean interaction; Surface observations; Turbulence; Pacific Ocean; Parameterization

1. Introduction

The direct covariance (DC) method is the most direct method of atmospheric turbulent flux estimation (Edson et al. 1998). Over the oceans, a relatively limited set of DC data have been used to develop bulk flux algorithms. These algorithms are used in numerical models, satellite data, and analysis products to estimate surface fluxes from bulk quantities (e.g., 5–60-min-averaged sea surface temperature, air temperature, humidity, and wind speed), which are easier to measure and model than the

turbulent fluxes themselves. Some bulk flux algorithms are periodically updated as more DC data are collected (Fairall et al. 2003; Edson et al. 2013), although DC flux measurements remain spatiotemporally sparse. In this study we demonstrate the ability of Sailable uncrewed surface vehicles (USV) to routinely provide reliable DC flux measurements and thereby greatly increase the pool of data available to improve understanding of ocean surface fluxes and develop bulk flux algorithms.

Sailables are wind- and solar-powered USV equipped with suites of meteorological and oceanographic sensors. They are capable of operating in remote ocean areas for months at a time, returning some data in real time via satellite communication and providing the rest of the high-resolution record at recovery. The routinely collected data allow calculation of surface wind stress and sensible heat and buoyancy fluxes by the DC method. The DC wind stress is the focus of this work. Bulk method calculations of wind stress, buoyancy flux, and latent and sensible heat flux are also possible. The data analyzed here come from two missions in the tropical east Pacific in 2017, with two Sailables, and 2019, with four Sailables. The quality of data from the 2017 mission was established by Zhang et al. (2019), who compared several quantities with data from a nearby fixed mooring. Wills et al. (2021) present data from three tropical Pacific Sailable missions, for analysis of meteorological and oceanographic variability around

 Denotes content that is immediately available upon publication as open access.

 Supplemental information related to this paper is available at the Journals Online website: <https://doi.org/10.1175/JTECH-D-22-0077.s1>.

Reeves Eyre's current affiliation: ERT Inc., and NOAA/NWS/NCEP/Climate Prediction Center, College Park, Maryland.

Corresponding author: Jack Reeves Eyre, jack.reeveseyre@gmail.com

DOI: 10.1175/JTECH-D-22-0077.1

© 2023 American Meteorological Society. For information regarding reuse of this content and general copyright information, consult the [AMS Copyright Policy](#) (www.ametsoc.org/PUBSReuseLicenses).

thunderstorms in the intertropical convergence zone (ITCZ). Those studies, however, did not include DC fluxes, which is the focus of our work here.

The DC method is technically challenging—especially at sea. Several instrument challenges are common to both land and ocean settings, including the need to resolve relatively small fluctuations of multiple geophysical variables simultaneously and at high time resolution. For ocean settings, additional challenges arise from the motion of the platform and the possible distortion of the flow by the platform. Sensors that measure Sairdrone motion are used to correct for platform motion, but assessing the quality of this correction is difficult. Finally, for small uncrewed vehicles and buoys, power consumption and maintenance requirements limit the types of instruments which can reliably be used. The Sairdrones used in this study were equipped with Gill WindMaster sonic anemometers, but did not have separate high-frequency humidity sensors, so it was not possible to calculate DC moisture fluxes. As the instrument type used here is widely used on observing platforms and has well-known properties for DC measurements, the primary challenges in this setting are related to flow distortion and platform motion.

Flow distortion is most apparent in ship-based DC data, where the superstructure of large oceangoing research vessels can deflect the wind flow even in cases where the ship is facing directly into the wind and instruments are mounted near the bow (Prytherch et al. 2015). For smaller platforms like buoys, flow distortion is potentially less extreme than for large ships, but is still possible (Bigorre et al. 2013). In this context, Sairdrones are more akin to buoys than ships, due to their small size and slim profile. However, they do face a challenge that has not been addressed before in the DC literature: Sairdrones gain propulsion from the wind through means of a rigid “wing”-like sail which, by design, distorts the mean wind flow in order to extract energy from it. Like conventional sailboats, Sairdrones heel, meaning that the wing is often oriented away from vertical. This orientation may cause flow distortion due to deflection of horizontal flow to a nonzero mean vertical flow. With results presented below, we quantify flow distortion caused by the Sairdrone.

Wave- and wind-induced motion is unavoidable for any floating platform at sea, but is more pronounced for small and lightweight platforms like Sairdrones and buoys than for oceangoing research ships. Well-established methods (Edson et al. 1998; section 3b) are used as standard in Sairdrone’s onboard software to correct for the effects of motion and give wind components in an Earth-relative coordinate system. Understanding how well the correction works is made difficult by conditions prevalent in our study areas. The deep tropics, especially in the eastern Pacific, are often swell dominated (Hanley et al. 2010). The winds are light and the surface wave field is dominated by long-period waves generated by stronger winds elsewhere. In these conditions, the wind near the ocean surface can be forced by the waves, rather than the usual case of waves forced by wind. Therefore, the wind can include genuine wave-coherent perturbations (Högström et al. 2015). This means that the criterion used by Bourras et al. (2019) to compare motion correction methods—that they should remove all wave-coherent

motions from the wind spectrum—is not suitable in our case. Despite the absence of a clear indicator of accuracy for motion correction, investigations of the Sairdrone motion correction are presented below.

Estimating the effects of flow distortion and platform motion are important for understanding the resulting data and derived quantities. Ultimately, however, in order to establish Sairdrones as viable DC platforms, we need to demonstrate the quality of the wind stress measurements. Two methods are available to us here: comparison with other well-established DC platforms, and comparison with bulk wind stress from Sairdrone data. The comparison against another platform—one that has already been shown to provide reliable DC measurements—is the more independent test, but has shortcomings of likely short duration and uncertainty due to spatial separation (for safety reasons, Sairdrones usually maintain a separation of a few miles from other ships or buoys). Comparison with bulk data from Sairdrones themselves has advantages of long duration of comparison and spatial coincidence. However, other uncertainties are introduced by the bulk method itself. Further, the data used by the bulk method may be prone to systematic flow distortion and platform motion issues mentioned above, as well as inevitable random uncertainties. In our context, any discrepancy between DC and bulk wind stress measurements could in principle indicate one or more of the following: random measurement uncertainty in the DC input data, systematic errors in the DC input data, or shortcomings in the bulk algorithm or motion correction. Random measurement uncertainties are also possible in the input data to the bulk algorithm, but Zhang et al. (2019) show that such uncertainties are acceptably small. Because of the multiple, interrelated sources of uncertainty, it seems inevitable that establishing the quality of DC fluxes may always involve a degree of subjective judgment. Where possible, all sources of error in DC fluxes are considered and investigated in this paper.

Finally, we also analyze wind stress in the presence of strong currents. Studies using estimates of wind stress from in situ data (Edson et al. 2013) and satellite scatterometers (e.g., Chacko et al. 2022; Kelly et al. 2001) have shown that ocean currents have a significant impact on wind stress magnitude. DC wind stress estimates permit the investigation of ocean current impacts on wind stress direction. The Sairdrone missions analyzed here crossed two major bands of strong current: the eastward-flowing North Equatorial Countercurrent at around 8°N that typically opposes the trade winds and the westward-flowing South Equatorial Current centered on the equator. These current systems provide opportunities to understand the role of currents in establishing wind stress magnitude and direction. This analysis also presents another demonstration of Sairdrone’s ability to provide accurate DC wind stress estimates.

2. Data and methods

What follows is a description of the Sairdrone data, and the methods used to calculate DC and bulk wind stress from the Sairdrone input data.

a. Sairdrone data

We use data from three Sairdrone missions to/from and in the eastern tropical Pacific which were organized as part of a Tropical Pacific Observing System (TPOS) pilot project. In the first of these missions, two Sairdrones departed Alameda, California, in September 2017, focused on the equatorial region around 125°W, and returned to California in May 2018. For parts of this mission, the sonic anemometers ran in intermittent mode to save power, sampling for 1 min then switching to standby for 4 min, which precludes DC calculations for these periods. The second mission ran from October 2018 to February 2019 and is included in some of our analysis below to help shed light on motion correction and flow distortion. DC fluxes, however, were not calculated for this mission because it ran with anemometers mostly in intermittent mode. In the third mission, four Sairdrones departed Honolulu, Hawaii, in June 2019, headed south to the equator at around 140°W, and returned to Honolulu in December 2019.

Sairdrones are equipped with a wide range of sensors measuring near-surface atmospheric and oceanic properties (Zhang et al. 2019). Of primary interest here is the sonic anemometer (Fig. 1), which measures three-dimensional winds and sonic temperature. On the Sairdrones used here, the anemometers were mounted on a short extension pole at the top of the wing, at a height of approximately 5 m. During the 2017 mission, the anemometers sampled at 10 Hz continuously for about 4 months of the mission, and sampled intermittently for the rest of the time. During the 2019 mission, the anemometers sampled at 20 Hz continuously throughout the mission. Other Sairdrone measurements used in the study include the following:

- 1) Air temperature and humidity from a Rotronic HC2-S3. This a slow response instrument that takes ~ 10 s to respond to fluctuations in relative humidity and temperature. Therefore, it is used for the bulk flux calculation, but not for DC fluxes.
- 2) Sea surface temperature measured in situ at about 0.6 m depth. Data from downwelling solar and longwave radiometers were also used in the bulk flux algorithm to extrapolate the subsurface temperature measurement to a skin temperature following Fairall et al. (1996a).
- 3) Near-surface currents from an acoustic Doppler current profiler that returned depth-resolved currents from ~ 6 to 100 m. Note that the possibility of shear between the surface and 6 m leads to some uncertainty in the true surface current.
- 4) Three-dimensional platform accelerations and rotations from two independent inertial measurement units (VectorNav VN-300) on the wing and hull. These were used in real time for motion corrections and, for the 2019 mission, were post-processed to estimate wave significant height and dominant period.

b. Wind transformation and related notation

Sairdrone's onboard software performs motion correction in real time using an algorithm based on Edson et al. (1998).

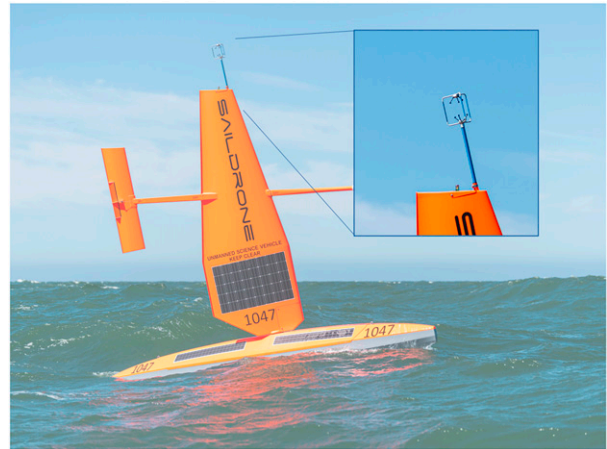


FIG. 1. Photo of a Sairdrone underway. Note that this is not one of the Sairdrones used in this study but is of the same type. The inset shows a close up of the sonic anemometer and mounting pole on top of the wing. Image: courtesy Sairdrone.

This algorithm aims to remove the effects of translation velocity, instantaneous tilt, and angular velocity. The algorithm takes as input the raw components in anemometer-relative coordinates and outputs the corrected wind components in the conventional meteorological (east–north–up) coordinates. Verification of the motion correction method follows in section 3. But first we pause to clarify notation for the wind and stress related vector quantities.

- 1) \mathbf{U}_{raw} : The three-dimensional vector representing airflow past the anemometer, in a frame of reference fixed with respect to the anemometer or, equally, with respect to the Sairdrone wing. We define basis vectors $(\hat{\mathbf{i}}_{\text{anem}}, \hat{\mathbf{j}}_{\text{anem}}, \hat{\mathbf{k}}_{\text{anem}})$ for the anemometer coordinate system. These vectors point backward, to the right, and up-wing (n.b., not vertical) from the anemometer, respectively. Then, we can write $\mathbf{U}_{\text{raw}} = u_{\text{raw}}\hat{\mathbf{i}}_{\text{anem}} + v_{\text{raw}}\hat{\mathbf{j}}_{\text{anem}} + w_{\text{raw}}\hat{\mathbf{k}}_{\text{anem}}$. These components correspond to Sairdrone's raw, uncorrected winds. For example, with the wing pointing into the wind u_{raw} is positive.
- 2) \mathbf{U} : The three-dimensional vector representing the true meteorological wind in a terrestrial reference frame (e.g., fixed with respect to land or the seabed). We define two coordinate systems that can be used to describe this reference frame. One uses basis vectors pointing east, north, and upward $(\hat{\mathbf{i}}_E, \hat{\mathbf{j}}_N, \hat{\mathbf{k}})$, so that $\mathbf{U} = u_E\hat{\mathbf{i}}_E + v_N\hat{\mathbf{j}}_N + w\hat{\mathbf{k}}$. These components correspond to Sairdrone's motion-corrected winds. The other possible coordinate system is the streamwise–crosswind coordinate system. This aligns the first horizontal component with the time-mean wind, and we define basis vectors $(\hat{\mathbf{i}}_x, \hat{\mathbf{j}}_y, \hat{\mathbf{k}})$. Then we can write $\mathbf{U} = u\hat{\mathbf{i}}_x + v\hat{\mathbf{j}}_y + w\hat{\mathbf{k}}$. This coordinate system is the one more commonly used in the DC flux literature. Note that the time mean of the v component, $\langle v \rangle$, is identically equal to zero in this case.
- 3) \mathbf{U}_{curr} : The two-dimensional vector representing the ocean surface current in a terrestrial reference frame. The current can be described in either of the terrestrial reference frames

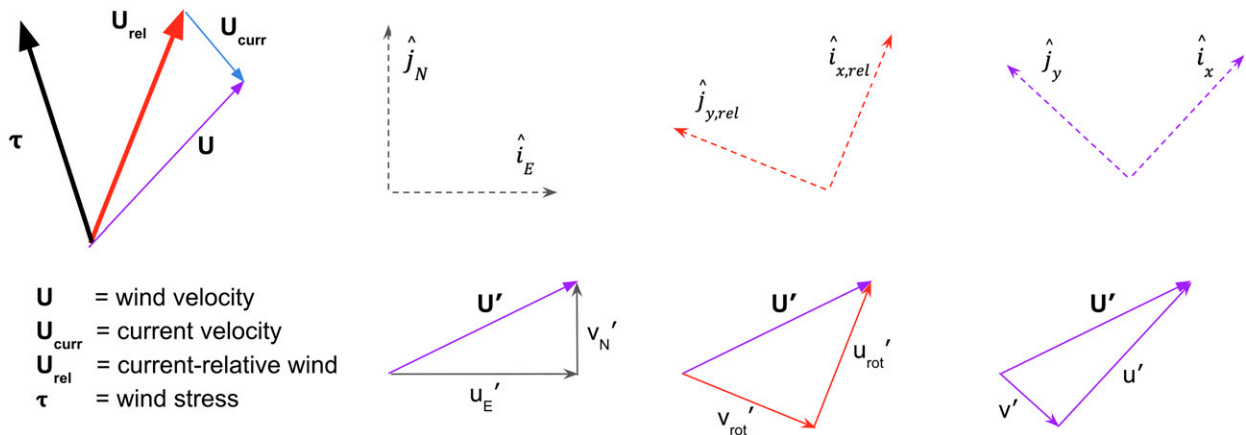


FIG. 2. Schematic showing wind, current, and wind stress vectors, and three coordinate systems based on them. Wind stress definition is discussed in section 2d. The decomposition of a generic instantaneous wind perturbation is shown below each of the three coordinate systems. Note that the stress and various wind vectors are not aligned in this schematic. This example is hypothetical though physically plausible, particularly under low winds.

noted above. Saildrones provide the data in east–north–up coordinates so $\mathbf{U}_{\text{curr}} = u_{\text{curr},E} \hat{\mathbf{i}}_E + v_{\text{curr},N} \hat{\mathbf{j}}_N (+ 0 \hat{\mathbf{k}})$.

- 4) $\mathbf{U}_{\text{rel}} = \mathbf{U} - \mathbf{U}_{\text{curr}}$: The three-dimensional vector representing the wind experienced by the moving ocean surface (neglecting wave motion). Also known as the current-relative wind. It is useful to define a coordinate system based on the current-relative wind analogous to the streamwise/cross-stream coordinate system for \mathbf{U} . We define basis vectors $(\hat{\mathbf{i}}_{x,\text{rel}}, \hat{\mathbf{j}}_{y,\text{rel}}, \hat{\mathbf{k}})$ and components $\mathbf{U}_{\text{rel}} = u_{\text{rel}} \hat{\mathbf{i}}_{x,\text{rel}} + v_{\text{rel}} \hat{\mathbf{j}}_{y,\text{rel}} + w \hat{\mathbf{k}}$ such that $\langle v_{\text{rel}} \rangle = 0$. It is also useful to be able to write the Earth-relative wind \mathbf{U} using these basis vectors: $\mathbf{U} = u_{\text{rot}} \hat{\mathbf{i}}_{x,\text{rel}} + v_{\text{rot}} \hat{\mathbf{j}}_{y,\text{rel}} + w \hat{\mathbf{k}}$.

These coordinate systems and vectors are shown schematically in Fig. 2. Two other quantities are used in the investigation of flow distortion. The motion-corrected wind tilt angle is $\arctan(w/\sqrt{u^2 + v^2})$. The anemometer’s relative wind direction is $\arctan(v_{\text{raw}}/u_{\text{raw}})$.

c. Quality control

The multimonth Saildrone missions produced a large volume of data. For example, the 20-Hz anemometer data from a single Saildrone in the 2019 mission contain nearly 300 million time steps and occupy over 40 GB of storage. The data volume causes difficulties in verifying the quality. We take the approach of using automated methods to find several common failure modes and we also manually flag questionable data where our investigations reveal them. We accept that this approach may well miss some episodes of bad data. We first apply the anemometers’ own status indicator, removing *all* wind components and sonic temperature when the status is anything other than functioning correctly. Spikes are detected using a median absolute deviation method [Mauder et al. 2013, their Eq. (1), but with $q = 5.0$ and 5-min time windows]. While this is not thought to be the most reliable (Starkenbug et al. 2016), it is computationally efficient and robust to missing values. We also found it to be satisfactory in the subset of cases that we

manually examined. Other problems detected intermittently in the data include GPS dropouts that can sometimes cause other records to be unrealistic. In all cases, when any wind component or sonic temperature was flagged, the others were also flagged. Whole 10-min averaging periods were excluded when more than 1% of the data were flagged. After removing flagged data, gaps of up to 1 s were filled using linear interpolation.

d. Direct covariance fluxes

After motion correction and quality control, the data are ready for the DC flux calculation. Within the DC calculation, however, there are a number of methodological choices to be made. These include whether the calculations are made in the time or frequency domain, the choice of averaging period, and the choice of wind stress coordinate system (Fig. 2).

The DC method uses the covariance between fluctuations about the mean of vertical wind speed and fluctuations about the mean of another quantity, to quantify the magnitude and direction of vertical transport by turbulent atmospheric eddies. The covariance can be most simply calculated using time series data. The covariance of two quantities is proportional to the slope of best-fit line in a scatterplot of the two quantities. The covariance can also be calculated as an integral over the cospectra of two quantities. This frequency domain calculation has the benefit of flexibility. Cospectra can be filtered to minimize spectral leakage and erroneous flux contributions from frequencies outside the estimated range of turbulent variations. Multiple consecutive cospectra can be averaged to reduce noise (though this can also be done in the time domain). However, the cost of these benefits is the added difficulty of applying the method to large datasets. The method is computationally more expensive and it requires more human intervention. For these reasons, we use the simpler time series calculation.

The DC method is sensitive to the choice of time period over which to calculate covariances. Periods are usually chosen from

the range 5–60 min. Shorter periods are desirable as they give higher-resolution output data. However, short periods have disadvantages of smaller signal-to-noise and the potential to miss important longer period fluctuations (i.e., the contribution from larger eddies). Conversely, longer periods can also be problematic in that they begin to sample larger-scale trends, including spatial gradients, mesoscale phenomena, and diurnal cycles, which bias the results. We use 10-min-averaging periods. This is something of a compromise but near the lower end of the usual 5–60-min range in order to obtain a higher-resolution output.

The final methodological choice we consider is the choice of wind stress direction assumptions. The choice is important for validation of Saildrone DC wind stress as it can affect comparison with other data sources and methods. It is common in the DC literature to use the coordinate system aligned with the current-relative wind. Using the coordinate systems discussed earlier for winds, the wind stress vector $\boldsymbol{\tau}$ can be written as $\boldsymbol{\tau} = \tau_{x,\text{rel}}\hat{\mathbf{x}}_{\text{rel}} + \tau_{y,\text{rel}}\hat{\mathbf{y}}_{\text{rel}}$ or as $\boldsymbol{\tau} = \tau_x\hat{\mathbf{x}} + \tau_y\hat{\mathbf{y}}$ or as $\boldsymbol{\tau} = \tau_E\hat{\mathbf{e}}_E + \tau_N\hat{\mathbf{e}}_N$. The vector wind stress is, by definition, the same in any case, but the partitioning into individual components differs. Some DC flux studies neglect the crosswind component and use the approximation $|\boldsymbol{\tau}| \approx \tau_x$ or $|\boldsymbol{\tau}| \approx \tau_{x,\text{rel}}$. The justification for this is that it reduces bias from the potentially noisy crosswind component when calculating the wind stress magnitude. However, this choice does assume that the wind stress is exactly in the direction of the mean relative wind. This assumption is somewhat problematic, especially in swell-dominated seas (Grachev et al. 2003). We revisit this topic in our analysis below, but for now we sidestep the issue by retaining all components. Regardless of which coordinate system is chosen, the DC calculation proceeds in a similar way:

$$\tau_E = -\rho_a \langle u'_E w' \rangle \quad \tau_N = -\rho_a \langle u'_N w' \rangle, \quad (1)$$

$$\tau_x = -\rho_a \langle u' w' \rangle \quad \tau_y = -\rho_a \langle v' w' \rangle, \quad (2)$$

$$\tau_{x,\text{rel}} = -\rho_a \langle u'_{\text{rot}} w' \rangle \quad \tau_{y,\text{rel}} = -\rho_a \langle v'_{\text{rot}} w' \rangle. \quad (3)$$

Here, the prime symbol represents the perturbation term in the Reynolds decomposition of a quantity. For example, $u = \langle u \rangle + u'$. Angle brackets are used to denote the 10-min mean of a quantity. Finally, we use drag coefficients derived from DC wind stress to compare with those derived from the bulk wind stress. We define

$$C_{D,\text{mag}} = \frac{|\boldsymbol{\tau}|}{\rho_a (u_{\text{rel}}^2 + v_{\text{rel}}^2)} \quad (4)$$

and

$$C_{D,\text{stream}} = \frac{\tau_{x,\text{rel}}}{\rho_a (u_{\text{rel}}^2 + v_{\text{rel}}^2)}. \quad (5)$$

Note that $|\boldsymbol{\tau}| = \sqrt{\tau_E^2 + \tau_N^2} = \sqrt{\tau_x^2 + \tau_y^2} = \sqrt{\tau_{x,\text{rel}}^2 + \tau_{y,\text{rel}}^2}$. A corollary of this is that $C_{D,\text{mag}} \geq C_{D,\text{stream}}$ and, in practical terms, $C_{D,\text{mag}} > C_{D,\text{stream}}$ because $\tau_{y,\text{rel}}$ is always nonzero.

e. Bulk fluxes

In addition to the DC wind stress calculation already discussed, we also use the Saildrone data to calculate fluxes using

the bulk method. This allows comparison between the two methods and also provides latent and sensible heat fluxes (both of which contribute to the buoyancy flux). It is worth noting here that we do not use inertial dissipation (ID) fluxes in this study. This could provide a third method for comparison with bulk and DC wind stress—one which is less sensitive to platform motion than the DC method (Fairall et al. 1990). Our main reason for not using the ID method is that it is less direct than the DC method, relying on several assumptions and empirical functions (Janssen 1999). In particular, the ID method may be unsuitable when applied within the wave boundary layer in developing seas and swell conditions (Donelan et al. 1997; Edson and Fairall 1998). This is because kinetic energy exchange between the water surface and atmosphere result in a departure from the assumed relationship between turbulent dissipation and wind stress. The ID method is also unable to provide an independent wind stress direction, limiting its usefulness in our study of strong currents and swell. Recent updates to the COARE algorithm have used DC wind stress exclusively (Edson et al. 2013). Therefore, it seems that DC fluxes are the most valuable source of data to support research into ocean surface fluxes.

For the bulk fluxes, we use the COARE version 3.5 algorithm (Fairall et al. 1996b,a, 1997, 2003; Edson et al. 2013) with wind speed-dependent roughness length, and sea surface temperature corrections based on diurnal warming and cool-skin effects. In the low-wind ($<5 \text{ m s}^{-1}$) conditions common in the eastern tropical Pacific, it is important to include wind adjustments due to gustiness and surface currents. Near-surface (6+ m) currents are obtained from the Saildrones' acoustic Doppler current profilers. Gustiness due to boundary layer-scale large eddies is included through an empirical coefficient which makes use of an adjustable parameter β , which we set to 1.25 [see Eq. (8) in Fairall et al. 2003]. The COARE algorithm is used to calculate streamwise, i.e., along-wind, wind stress magnitude. The wind stress direction is assumed to be the same as \mathbf{U}_{rel} . Among other parameters, COARE also outputs Obukhov length, drag coefficient, and SST diurnal warm layer and cool skin adjustments.

The data required by the COARE v3.5 algorithm include current-relative wind speed, air temperature, and humidity, near-surface seawater temperature, sea surface current velocity, the depths and heights of all measurements, and, for diurnal warm layer and cool skin adjustment, shortwave and longwave radiation. We use the COARE algorithm with 10-min averages of these inputs, resulting in 10-min-average fluxes that match the resolution of the DC results. Quality control on the inputs was completed by manual inspection to remove unrealistic values and periods with suspiciously large or small variability.

3. Results

a. Flow distortion and platform motion

It is common in DC calculations to filter out data when the wind is blowing from unfavorable directions relative to the ship or buoy structure. For example, one approach, for ships with the anemometer mounted near the bow, is to retain only

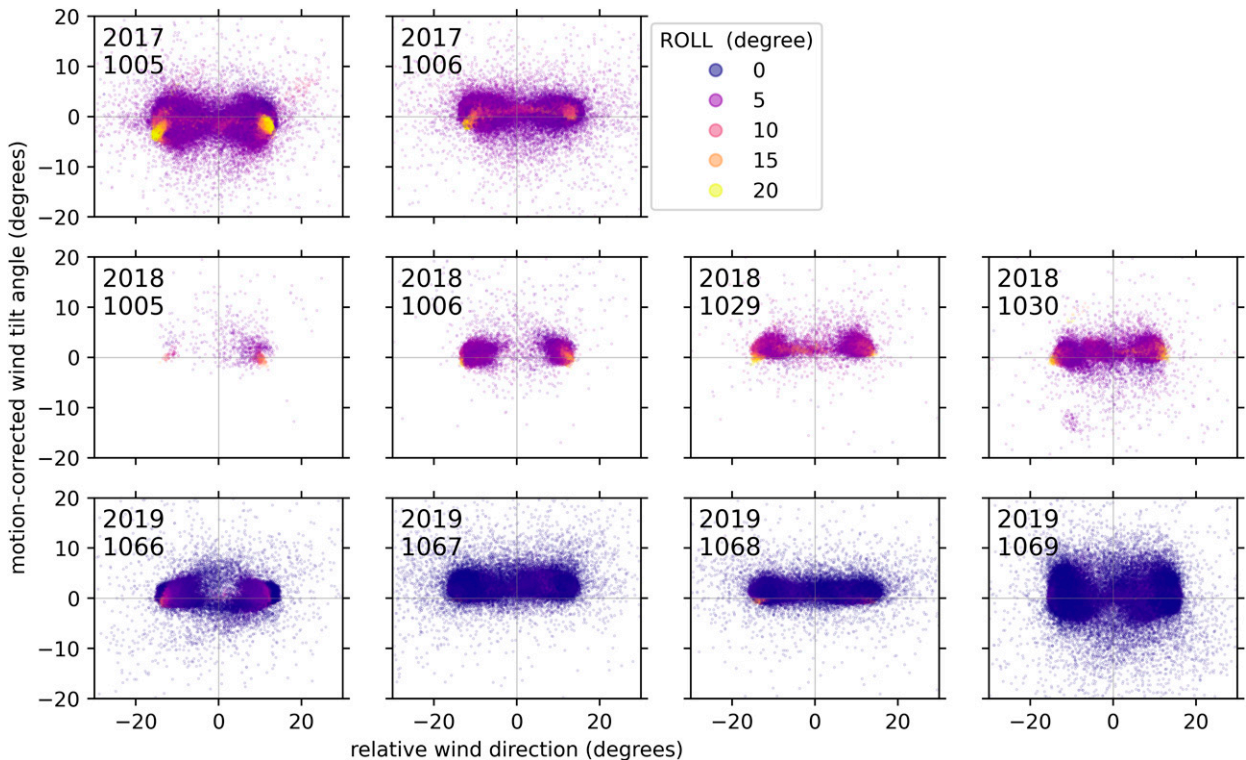


FIG. 3. Scatterplots of wind tilt angle against relative wind direction. Positive tilt angle represents upward air motion. Each small point represents a 1-min mean, colored by hull roll angle. There is one panel per SAILDRONE, grouped in rows by mission year: (top) 2017, (middle) 2018, and (bottom) 2019. The numbers in each panel show the year and SAILDRONE ID.

data from periods when the relative wind direction (see definition at the end of section 2b) is within 90° of directly forward. While SAILDRONES have a relatively slim and clean profile compared to a research ship, it is still important to check for any similar effects. We analyze this by looking at the relationship between relative wind direction and wind tilt angle (Fig. 3). The vast majority of data points have a relative wind direction within $\pm 20^\circ$. This happens because the anemometer rotates with the SAILDRONE wing, which is designed to operate within a narrow range of relative wind directions for sailing efficiency. The wind tilt angle does not have an obvious dependence on relative wind angle. This suggests that SAILDRONES, by virtue of their rotating wing and anemometer, do not need filtering based on wind directions in the way that ships do. There are minor differences between SAILDRONES in terms of their mean wind tilt, which may reflect differences in anemometer calibration or orientation. Even so, most points have tilts of less than 5° in absolute value, which is at or below the tilt angle measured on ships. Many of the points with higher tilt angles, greater than 10° for example, occur with low wind speeds when the tilt angle calculation is quite unreliable. Note that Fig. 3 does not imply that there is no flow distortion, only that flow distortion is similar across the range of observed relative wind directions.

We noted in the introduction that SAILDRONES have a unique potential form of flow distortion caused by the wing. Such flow distortion could affect both the mean wind (e.g., by deflecting the flow away from horizontal) and the turbulent deviations. We

focus on the mean wind flow distortion, and look for a signature that depends on the heel angle of the SAILDRONE. Figure 4 shows the vertical wind speed in relation to platform heel or roll angle (rotation around a horizontal axis joining bow to stern). Note that the smaller range of roll angles in the 2019 mission, compared to 2017 and 2018, is thought to be caused by a slightly heavier keel used on the newer generation of SAILDRONES, including 1066–1069. Contrary to our original hypothesis, the results in Fig. 4 show that, as a SAILDRONE heels, the wing deflects the wind downward. There are clear differences between different SAILDRONES, but the general pattern is that larger roll angles correspond to more negative vertical velocities. We conjecture that this pattern of vertical velocities may be caused by a wing-tip vortex forming over the end of the wing. Most of the 1-min-average vertical velocities are between -0.5 and 0.5 m s^{-1} which corresponds to flow tilts of 1° – 2° from horizontal. SAILDRONES 1005 in 2017 and 1067 in 2019 seem to have a larger gradient of vertical wind speed than others, possibly pointing to a slight offset from vertical in the sensor's installed orientation. SAILDRONES 1029 and 1030 in 2018 were equipped with larger wings, in an attempt to achieve better sailing abilities in the light winds of the tropics. This may explain their slightly different distribution of vertical wind speeds. For the missions we are using in most of our analysis, namely, 2017 and 2019, the degree of flow distortion generally seems to be quite minor compared to the vertical wind speed spread, and so we do not correct for it.

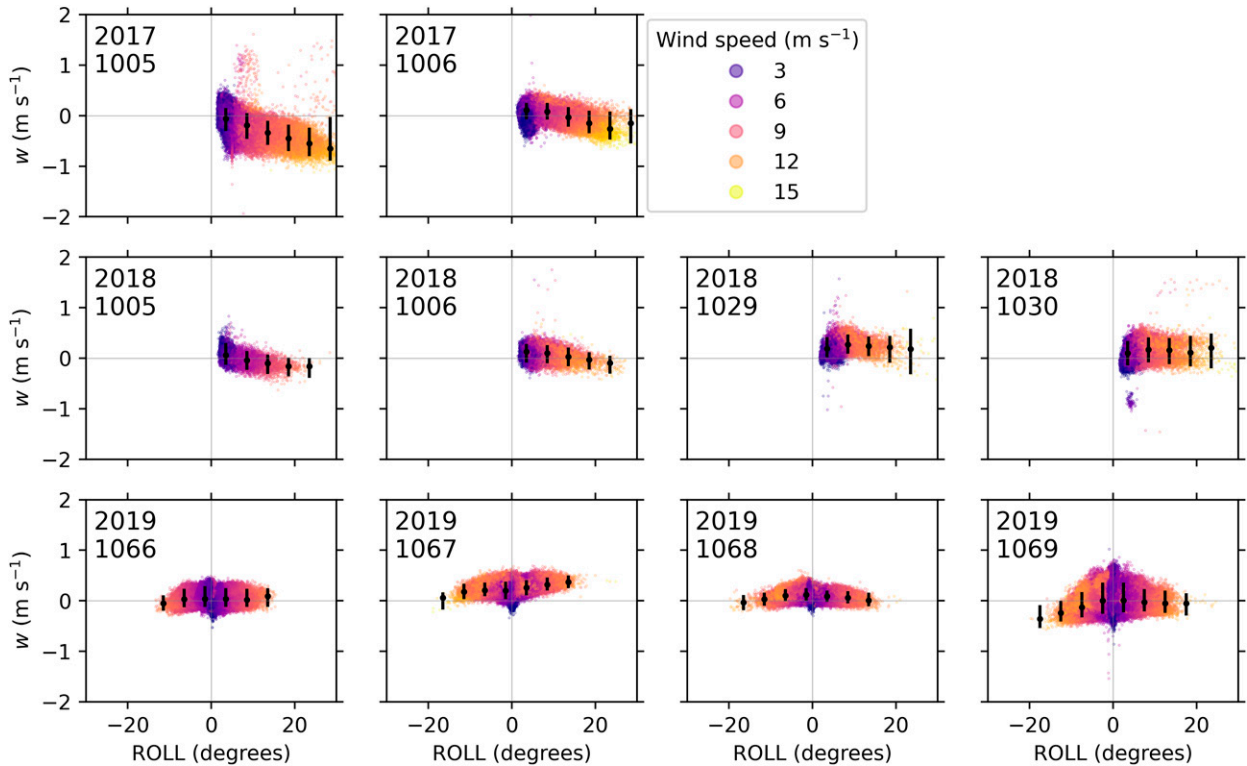


FIG. 4. Scatterplots of vertical wind speed against SAILDRONE hull roll angle. Positive vertical wind speed represents upward air motion. Roll represents the rotation angle of the SAILDRONE hull about the bow-to-stern axis. Each small point represents a 1-min mean, colored by horizontal wind speed. Large black points and bars represent the median and 5th and 95th percentiles of flow tilt in 5° roll bins. There is one panel per SAILDRONE, grouped in rows by mission year: (top) 2017, (middle) 2018, and (bottom) 2019. The numbers in each panel show the year and SAILDRONE ID. For 2017 and 2018, the absolute value of roll was measured without direction; in 2019 the direction [heeling toward port (negative) or starboard (positive)] was also measured.

We next try to verify the accuracy of the motion correction procedures by looking at spectra of corrected and uncorrected winds and platform motion (Fig. 5). Across the eight periods shown, the w_{raw} spectral intensity tends to peak around 0.2–0.3 Hz. The w flattens out this spectrum into something that better resembles the expected behavior in the inertial sub-range. However, the motion correction also seems to introduce new peaks. At around 0.07–0.1 Hz, the corrected vertical wind and SAILDRONE vertical velocity both show peaks, while the raw vertical wind does not. This suggests that the motion correction is adding in a vertical wind feature that coincides with the lowest-frequency peak in the platform motion spectrum, likely caused by surface waves, especially swell. Interestingly, the low-frequency alignment of w and \dot{z}_{SD} spectra is almost entirely absent in the strongest wind cases (Figs. 5b,f), and arguably strongest in light-wind cases. This agrees with the results of Soloviev and Kudryavtsev (2010) and Grare et al. (2018). However, similar behavior in Bourras et al. (2019, their Fig. 3) was deemed to be unrealistic and the authors chose to suppress “any vertical wind fluctuation that would be spectrally coherent with the vertical platform motion.” We feel that this condition is overly strict, especially in tropical regions where swell-dominated light-wind conditions commonly occur, causing wave-coherent wind fluctuations (Prytherch et al.

2015; Sullivan and McWilliams 2010). In summary, the motion correction seems to be sufficient to correct the wind spectra in the inertial sub-range, but has a relatively light touch, compared to approaches that remove all wave-coherent wind oscillations (e.g., Bourras et al. 2019) for lower-frequency oscillations. We suggest this is appropriate for swell conditions.

Figure 5 has two other features of note. First, all events have a peak in the platform motion spectra at 5 Hz, likely caused by a vibration in the SAILDRONE wing or the anemometer mounting to the wing. This is thought not to be significant for flux calculations as such a high frequency contributes little to the covariances (e.g., Edson et al. 1998, Fig. 9). Second, all spectra have their peak in w_{raw} at a surprisingly consistent frequency—around 0.25 Hz. As noted above, the motion correction seems to reliably smooth out this peak. Its cause is not known definitively but may be related to a resonant frequency in the SAILDRONE motion—for example, heave corresponding to a buoyancy frequency or pitch related to moment of inertia.

b. Direct covariance wind stress

The amount of DC data collected in the 2017 and 2019 missions is considerable (Table 1): over 100 000 flux averaging periods (10 min), which is equivalent to over 700 days or just under 2 years. Most of this is from 2019, when the four SAILDRONES also

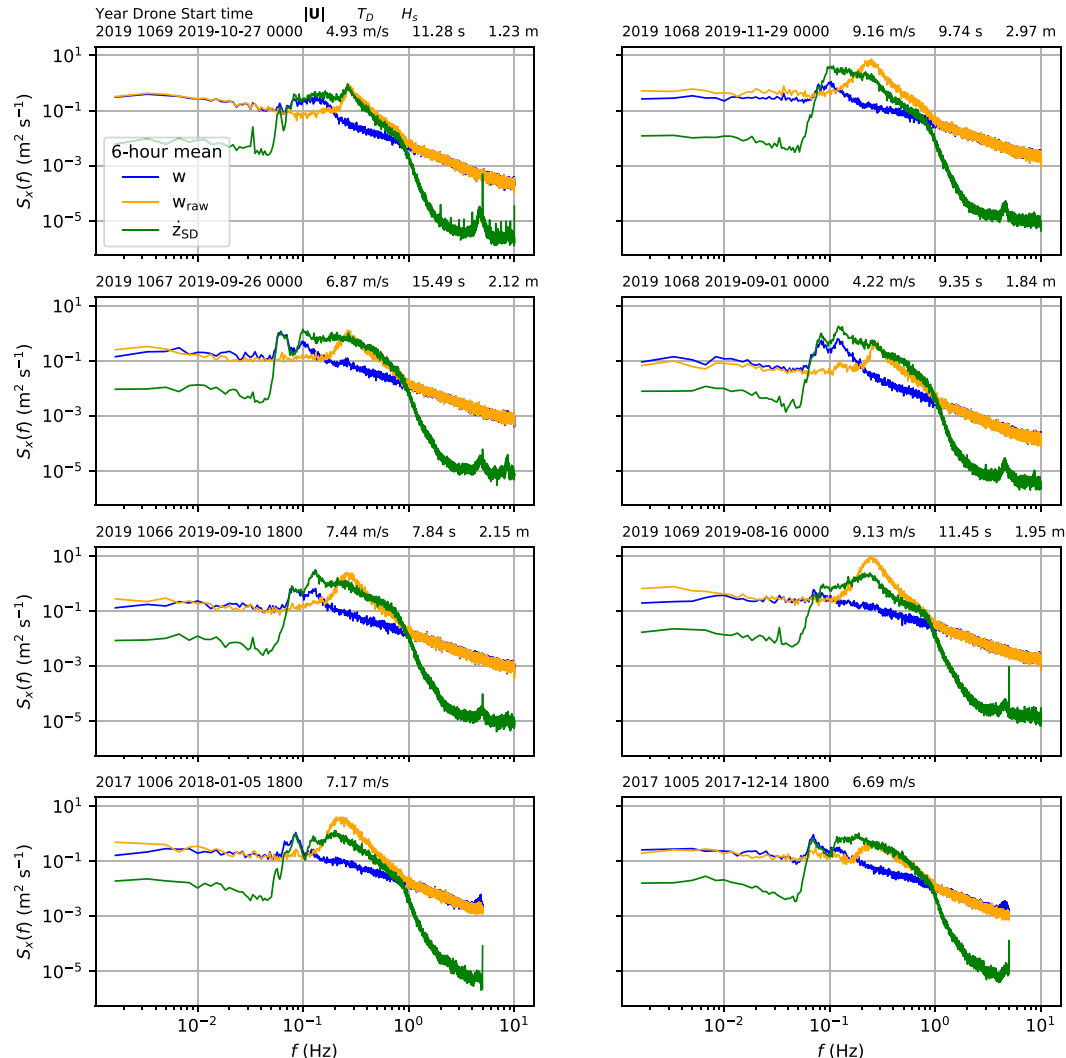


FIG. 5. Averaged power spectra of vertical wind fluctuations (with and without motion corrections) and Sairdron vertical velocity fluctuations for eight 6-h periods (one per panel). Motion-corrected vertical wind (w) is shown in blue; uncorrected vertical wind (w_{raw}) is shown in orange; Sairdron vertical velocity (\dot{z}_{SD}) is shown in green. All three quantities are detrended and tapered (using a Tukey window, which leaves the central 80% of each window unchanged) before calculation of spectra. Each spectrum shows the average of 37 ten-minute spectra (representing just over 6 h). Periods were selected to have consistent wind speed and direction in order to reduce noise in the spectra. The date, Sairdron ID, start time, average wind speed, and (where available) wave dominant period and significant height are shown above each panel. Note the logarithmic scales on each axis.

recorded surface wave data, giving over 500 days of combined DC and bulk wind stress data alongside wave data.

To assess the quality of our DC wind stress measurements, we compare them with coincident estimates based on the bulk method (Table 2). The Sairdron data fields used in the bulk algorithm were shown to be of high quality by Zhang et al. (2019), who compared 2017 Sairdron results with data from a mooring in the eastern tropical Pacific. Thus, the bulk wind stress results provide a reliable first assessment of the DC results. DC $|\tau|$ is on average greater than the bulk magnitude by $1.79 \times 10^{-3} \text{ N m}^{-2}$. The mean wind stress is of order 0.1 N m^{-2} so this represents a $\sim 2\%$ mean difference. Using

DC τ_x or $\tau_{x,\text{rel}}$ as the basis of comparison results in a mean difference that is one to two orders of magnitude smaller. This likely reflects the fact that the COARE algorithm used here was calibrated with DC $\tau_{x,\text{rel}}$, and so the algorithm is designed to only estimate the streamwise component of stress. The root-mean-square differences (RMSD) and mean absolute differences, relative to τ_{bulk} , are similar for all versions of the DC wind stress. The mean τ_{bulk} across the six Sairdrones included here is 0.072 N m^{-2} . Dividing the RMSD by the mean of τ_{bulk} gives an estimated uncertainty of 31.4% for $|\tau|$, and slightly smaller for τ_x and $\tau_{x,\text{rel}}$. This is comparable with results from Edson et al. (2013).

TABLE 1. Count of 10-min periods with valid DC data, individually and coincident with other data types (bulk wind stress, waves) from individual Saildrones and in total. DC data are classed as complete when they have 99% nonmissing data points. Wave data were not provided from the 2017 mission.

Year	Drone ID	DC	DC + bulk	... + currents	... + waves
2017	1005	14 927	14 581	14 029	0
	1006	15 746	15 287	14 891	0
2019	1066	10 940	10 886	10 886	10 879
	1067	22 643	22 509	22 509	22 495
	1068	22 508	22 495	22 483	22 474
	1069	17 606	17 604	17 598	17 587
	Total	104 370	103 362	102 396	73 435
Total (days)		724.8	717.8	711.1	510.0

An alternative presentation of the comparison between DC and bulk wind stress is given in Fig. 6, which shows over 5 months of data from a single Saildrone. The two time series match closely and it is difficult to see any systematic discrepancies. This remarkably good agreement, as quantified by Table 2, is an indicator that the Saildrone DC wind stress estimates are of high quality. Nonetheless, there are periods with a noticeable offset. For example, the bulk wind stress seems to exceed the DC for several days in late November (notice especially 26 and 29 November), while the DC exceeds the bulk on 10 August. Similar time series for other Saildrones are given in the online supplementary material.

Figure 7a shows data from all Saildrones in the form of $C_{D,mag}$ as a function of wind speed. The format is similar to Fig. 6 from Edson et al. (2013), and the results are quite similar: a functional form with a minimum at approximately 4 m s^{-1} and relatively wide spread of points below 5 m s^{-1} . However, our binned results reveal an important difference: below 4 m s^{-1} , our DC results are markedly higher than the bulk wind stress results based on the COARE 3.5 algorithm presented in Edson et al. (2013). Figure 7b repeats this analysis with $C_{D,stream}$. In this case, we see better agreement between DC and bulk drag coefficients at low wind speeds ($|\mathbf{U}_{rel}| < 4 \text{ m s}^{-1}$). This result suggests that it is the low wind speed differences that cause the larger mean differences for $|\boldsymbol{\tau}|$ seen in Table 2.

c. Wind stress and current directions

The differences between $|\boldsymbol{\tau}|$ and $\tau_{x,rel}$ highlight the possibility, demonstrated by other studies (Grachev et al. 2003; Ortiz-Suslow et al. 2018), that the wind stress may not act in the direction of \mathbf{U} or \mathbf{U}_{rel} . We explore this by looking at the off-wind stress angle, that is, the angle between $\boldsymbol{\tau}$ and \mathbf{U}_{rel} , as a function of wind speed (Fig. 8). For wind speeds above 4 m s^{-1} the off-wind stress angles are mostly less than 22.5° . For wind speeds less than 4 m s^{-1} , however, a significant fraction of off-wind stress angles are greater than 45° . For wind speeds less than 2 m s^{-1} , the off-wind stress angles are essentially uniformly distributed and there is no relationship between the wind stress direction and the relative wind direction.

TABLE 2. Error statistics for DC wind stress relative to bulk wind stress. These statistics average over all Saildrones in both missions. RMSD = root-mean-square difference. MAD = mean absolute difference. The number of observations is the same for all categories: 102 396 ten-minute periods.

Wind stress type	Mean difference	RMSD (N m^{-2})	MAD
$ \boldsymbol{\tau} - \tau_{bulk}$	1.79×10^{-3}	2.26×10^{-2}	1.36×10^{-2}
$\tau_x - \tau_{bulk}$	5.45×10^{-5}	2.20×10^{-2}	1.36×10^{-2}
$\tau_{x,rel} - \tau_{bulk}$	7.74×10^{-5}	2.20×10^{-2}	1.36×10^{-2}

Grachev et al. (2003) and Geernaert et al. (1993) show that off-wind stress angle is affected by swell propagating at an angle to the wind. Saildrones do not provide directional wave information, so we are unable to investigate whether the swell direction is responsible for the wind stress direction in our dataset. A further complication comes from the fact that our DC wind stress estimates come from a single anemometer at a fixed height. Wave-coherent wind fluctuations exhibit a strong vertical gradient whose features depend on wind and wave conditions (Grare et al. 2018; Soloviev and Kudryavtsev 2010). The existence of near-surface constant flux layer, assumed by Monin–Obukhov similarity theory, has even been questioned (Ortiz-Suslow et al. 2021). Quantifying where a Saildrone’s anemometer sits in such time-dependent near-surface vertical gradients is necessary to fully understand how well the DC wind stress estimates represent the stress at the ocean surface. However, this is beyond the scope of this paper. The nondirectional wave information that is provided by Saildrones does not suggest an obvious relationship between off-wind stress angles and either significant height or dominant period. However, we do note that among data points with wind speeds in the range $6\text{--}10 \text{ m s}^{-1}$, those with the largest off-wind stress angles tend to have large significant wave heights.

Figure 8 uses \mathbf{U}_{rel} for both magnitude in the independent variable and direction in the dependent variable. We expect that the direction of $\boldsymbol{\tau}$ is more closely related to the direction of \mathbf{U}_{rel} than to the direction of \mathbf{U} , and indeed this is assumed to be the case in bulk flux algorithms. Figure 9 shows a case where the assumption does seem to hold. The case features light winds in the north equatorial counter current region. Vectors show an eastward current and southerly wind, which combine to give a north-northwestward relative wind. The wind stress vector $\boldsymbol{\tau}$ is directed to the northwest, which is closer in direction to \mathbf{U}_{rel} than to \mathbf{U} . As has been shown previously for wind stress magnitude, this demonstrates the importance for wind stress direction of including ocean currents in stress calculations. However, noting that the Saildrone surface current measurement is at around 6 m, it is uncertain how much near-surface current shear may affect this result.

To investigate the effect of wind stress direction assumptions on the *magnitudes* of the DC wind stress, we generalized the streamwise stress calculation to any arbitrary direction, as opposed to the usual current-relative wind direction. The steps in the streamwise stress calculation are 1) rotation of coordinate system, 2) calculation of two orthogonal components of stress, and then 3) retention of only one component. The

2019, SD 1068

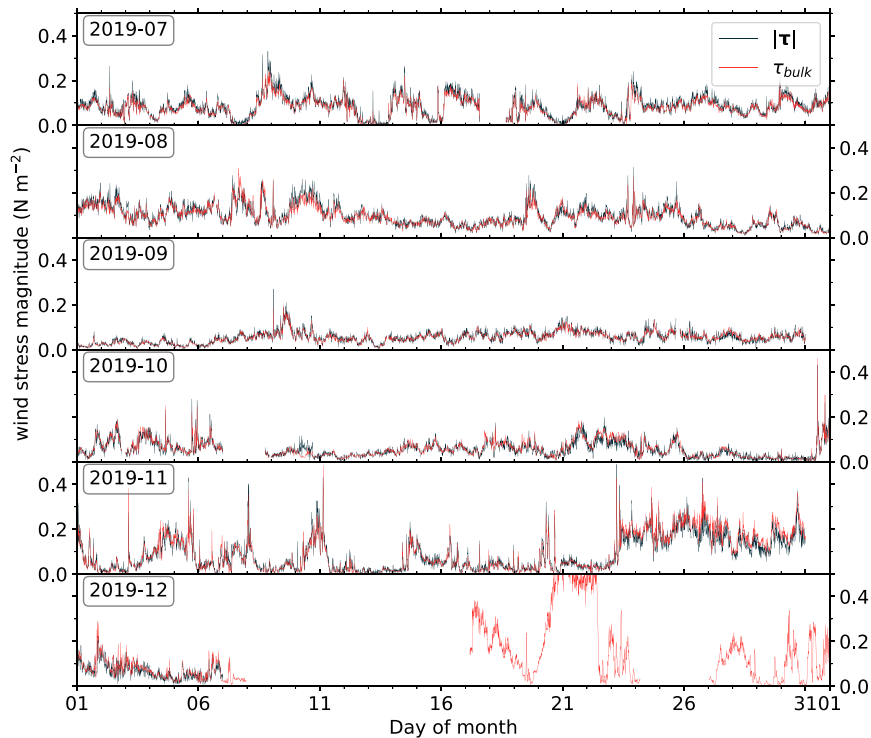


FIG. 6. Time series of wind stress magnitude from SAILDRONE 1068 in the 2019 mission. Bulk wind stress is red and DC wind stress $|\tau|$ is black. Each row represents 1 month of data. Bulk wind stress from 17 Dec onward is from tests at the end of the mission close to Hawaii; DC wind stress was not calculated for this period.

outcome of the generalization is shown by the dashed black lines in Fig. 9, which form two circular lobes. Mathematical manipulation of the covariance definitions under a rotation of axes demonstrates that the streamwise component of stress (τ_α) defined at any angle α to τ is given by $\tau_\alpha = |\tau| \cos \alpha$. (Of course, the value of α is usually unknown and effectively aligns with the wind or relative wind.) What this means is that the differences in magnitude between $|\tau|$ and $\tau_{x,rel}$ are uniquely determined by the angle between τ and \mathbf{U}_{rel} . For example, using the streamwise wind stress component in the direction of the wind (τ_x) in Fig. 9 would give a magnitude slightly over half of $|\tau|$.

In the case shown in Fig. 9, τ aligns more closely with \mathbf{U}_{rel} than \mathbf{U} . This also means that $\tau_{x,rel}$ is closer than τ_x to $|\tau|$. We next ask whether this holds more generally. Figure 10 shows the ratios of magnitudes of the different wind stress magnitudes for all cases where the current speed is at least half of the wind speed. We see that $\tau_{x,rel}$ is on average 69% of $|\tau|$, while τ_x is on average 63% of $|\tau|$. The distribution of differences has a definite positive skew and shows that, on average for the cases analyzed here, using $\tau_{x,rel}$ gives a wind stress around 10% larger than τ_x . The spread is considerable, however, so the difference often exceeds 25%, but also can be negative. By the reasoning discussed earlier, this analysis also implies that there is a better general angular alignment between τ and \mathbf{U}_{rel} than between τ and \mathbf{U} .

4. Discussion

Verification of DC measurements at sea is difficult. The best case is comparison with a nearby alternative platform known to provide accurate DC fluxes, though even this is made difficult by issues like spatiotemporal variability, instrument errors or differences, and methodological differences. Such a comparison is not possible for the SAILDRONE missions presented here, so we have turned to the next best thing: comparison with bulk fluxes from SAILDRONES themselves. The SAILDRONE data we use in the bulk algorithm have already been compared with a well-established buoy measurement system (in Zhang et al. 2019), which lends confidence that the bulk measurements are reliable. In our analysis here, the excellent agreement between bulk and DC wind stress estimates leads us to suggest that the DC stress estimates should be considered accurate to within community accepted standards (Cronin et al. 2019). From an operational perspective, given the relative simplicity of the DC calculation, we expect that the DC wind stress could be calculated and broadcast in real time.

One of the main results we have shown is the potentially large differences in DC stress estimates, at low wind speeds, between different direction assumptions. We have shown that calculating the DC wind stress as the streamwise component, $\tau_{x,rel}$, in the direction of \mathbf{U}_{rel} , can give significantly smaller

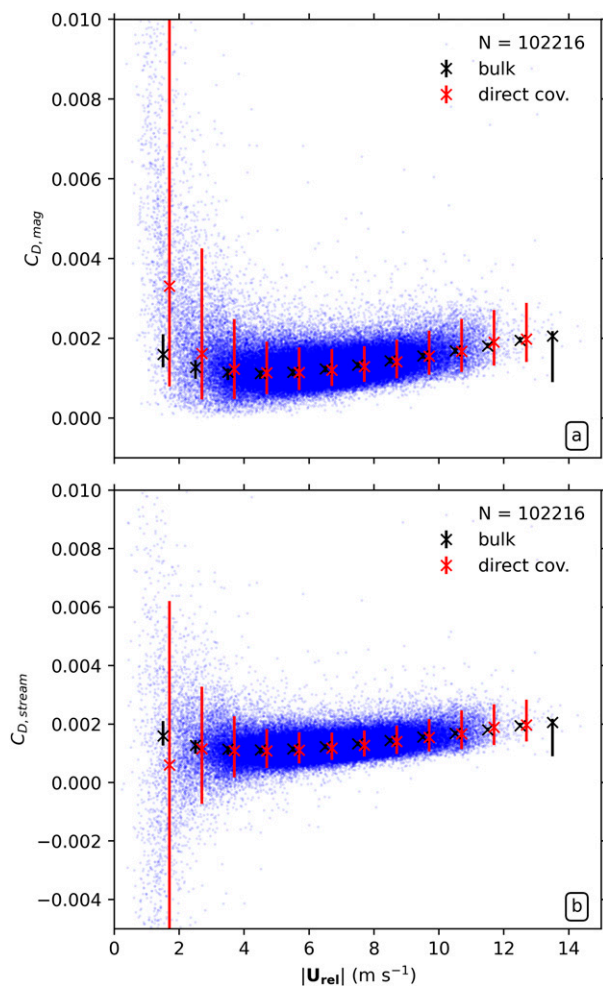


FIG. 7. Scatterplot of drag coefficient against current-relative wind speed: (top) $C_{D,mag}$ [see Eq. (4)]; (bottom) $C_{D,stream}$, calculated from $\tau_{x,rel}$ [see Eq. (5)]. Each blue point represents a 10-min-average DC value. The red crosses and bars represent the median and 5th and 95th percentiles of 1 m s^{-1} bins of the DC data. The black crosses and bars represent the same statistics for the bulk algorithm calculation of drag coefficient (individual data points not shown). The DC binned data have been slightly displaced to the right of the bin centers to aid legibility.

wind stress than using the magnitude of the vector wind stress $|\tau|$. This is because \mathbf{U}_{rel} and τ can point in different directions, and the magnitude differences are related by simple trigonometry to the directional differences. The differences raise two important questions: First, from an observational perspective, which is the more reliable DC stress direction? And second, are any changes warranted to the design of bulk flux algorithms?

On the first question, numerous studies (e.g., Grachev et al. 2003; Geernaert et al. 1993) have shown that, in cases of light winds and swell-dominated surface wave fields, the direction of τ can be significantly different to \mathbf{U}_{rel} . The DC wind stress estimates presented here support this. Wind directions also tend to be relatively variable in light winds, which can cause

further mismatch between directions of τ and \mathbf{U}_{rel} . For example, if wind speed fluctuations correlate with wind direction fluctuations, τ may be closer in direction to the wind direction of the stronger wind subperiods rather than the mean wind direction of the entire 10-min period. Thus, it is clearly advantageous to have a DC wind stress direction independent of the direction of \mathbf{U}_{rel} . However, errors and uncertainties in wind measurements and motion correction are, in a relative sense, large for light-wind conditions—the cases when choice of direction convention makes the biggest difference. It is possible, in these cases, for the sampling uncertainty to be on the same order of magnitude as the true mean wind stress. Therefore, adding the two DC stress components in quadrature to get $|\tau|$ results in overestimation of the true wind stress magnitude. On the other hand, making the approximation $|\tau| \approx \tau_{x,rel}$ results in underestimation of the true wind stress magnitude by an amount that depends on the angle between the true wind stress and \mathbf{U}_{rel} . Directional wave information could help assess whether swell effects explain the misalignment between τ and \mathbf{U}_{rel} . Unfortunately, Saildrones do not currently provide directional wave information. Global wave analyses may give useful information on the subject, but that investigation is beyond the scope of this study.

The second question—whether changes are warranted in bulk flux algorithms—must address the purposes of these algorithms. Whether for use in numerical models or driven by observations of bulk properties, bulk flux algorithms must often work on a limited number of variables. For the direction, \mathbf{U}_{rel} (or sometimes, if no current data are available, simply \mathbf{U}) is usually the only vector direction provided so there are no grounds to specify an alternative direction for the wind stress. In cases with wind speeds over 4 m s^{-1} , the wind stress direction error in using \mathbf{U}_{rel} is likely to be small. For the wind stress magnitude, the issue becomes then whether to tune the drag coefficient parameterization based on DC $|\tau|$ (in which case the bulk algorithm may overestimate $\tau_{x,rel}$) or based on DC $\tau_{x,rel}$ (in which case the bulk algorithm may underestimate $|\tau|$). COARE and some other bulk flux algorithms (e.g., Large and Pond 1981; Zeng et al. 1998) use $\tau_{x,rel}$. The decision potentially has small but important consequences for forcing of horizontal currents, vertical motion, and mixing in ocean models. Estimates of sensible and latent heat flux may also be affected, though recent work suggests the resulting change would be minor (Iyer et al. 2022). Any changes to the stress methodology would also require reconsideration of the parameterization of “gustiness” due to boundary layer-scale eddies.

The preceding discussion highlights a number of trade-offs that must be made when calculating wind stress. Longer averaging periods increase the signal-to-noise ratio, but require a statistical gustiness estimate to compensate for differences between instantaneous and time-averaged vector magnitudes (Cronin et al. 2006). Similarly, neglecting the cross-stream DC wind stress can increase the signal-to-noise ratio, but at the expense of a possible systematic underestimate of wind stress magnitude. The best choices are context dependent; for example, looking at vertical mixing in a one-dimensional ocean model may require different trade-offs to global analysis of vector wind stress from satellite data.

2019, SD 1068

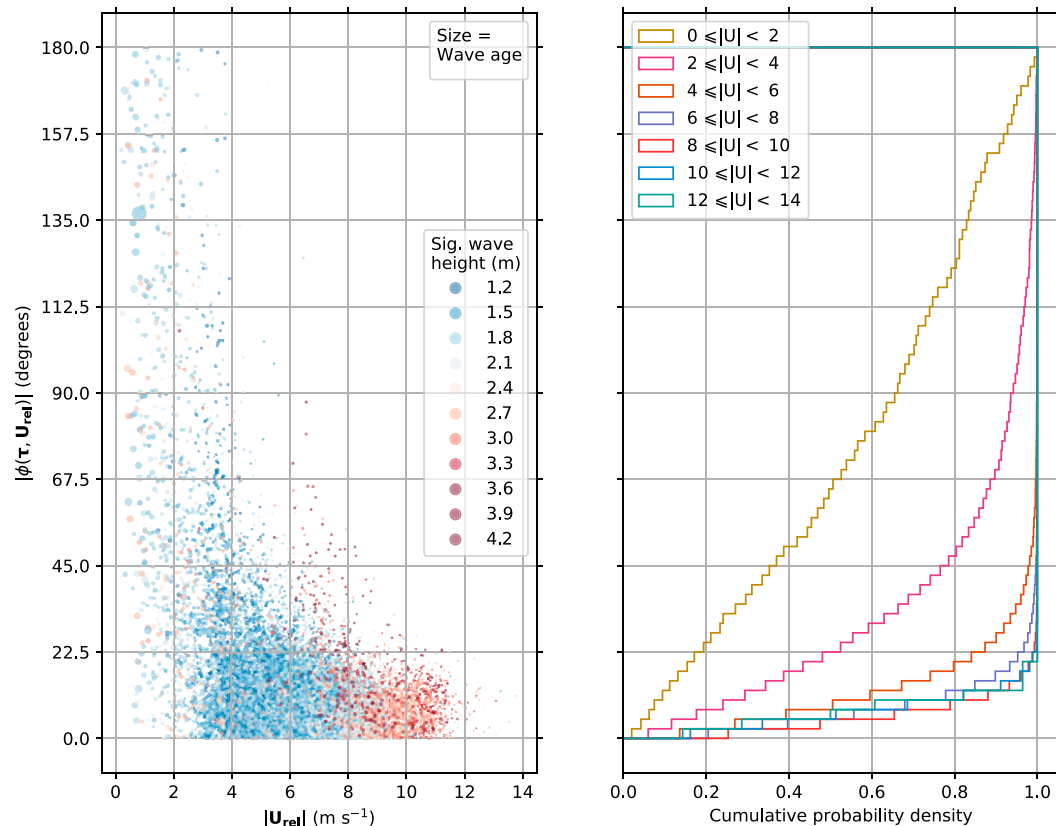


FIG. 8. Difference in direction (denoted ϕ) between wind stress (τ) and current-relative wind vector \mathbf{U}_{rel} shown as (left) scatterplot as a function of current-relative wind speed ($|\mathbf{U}_{rel}|$); (right) cumulative distribution functions for 2 m s^{-1} bins of current-relative wind speed. Points in the scatterplot are colored according to significant wave height and sized according to wave period (larger points corresponding to long-period swell or mature wind seas, and smaller points corresponding to short-period young wind seas).

Our results show that, when available, \mathbf{U}_{rel} should be used in preference to \mathbf{U} for the direction of the wind stress, in both bulk and DC methods. This is most important when the current is fast relative to the wind, which is not uncommon in the tropics or other locations in certain seasons. In one case presented here from the North Equatorial Countercurrent in the eastern tropical Pacific Ocean, this results in a change from $\tau_x \approx 0.5 |\tau|$ for Earth-relative winds to $\tau_{x,rel} \approx 0.9 |\tau|$ for current-relative winds. \mathbf{U}_{rel} is also more closely aligned with the vector wind stress τ . Averaging over a larger number of strong current cases, the increase in stress and closer alignment are not as large, but still significant ($p = 0.027$ in a two-sided, two-sample Kolmogorov–Smirnov test). We argue that this gives further credibility to the wind stress direction being a meaningful quantity independent of the wind direction, because if the DC wind stress direction was truly random and dominated by measurement error, then the chances of observing such a systematic result would be small.

In our analysis and discussion of the role of currents in wind stress direction, we have mostly focused on light-wind

situations. This is for two reasons: first, light-wind cases are when the greatest misalignment between \mathbf{U} and \mathbf{U}_{rel} occurs; and second, light-wind cases are when the greatest misalignment between τ and \mathbf{U}_{rel} , and therefore when the greatest difference between $|\tau|$ and $\tau_{x,rel}$, occurs. However, it is important to note that currents still play a role at high wind speeds through wind stress curl effects. Because atmospheric winds vary at relatively large scales, it is the current variation across ocean eddies that controls the wind stress curl. Thus, spatial variations of current and wind stress direction affect eddy-induced upwelling (Gaupe et al. 2015) and eddy kinetic energy (Renault et al. 2016).

5. Conclusions

We have calculated direct covariance (DC) wind stress from six Saildrones on two missions in the eastern tropical Pacific ocean. The results on average agree very well with COARE version 3.5 estimates of wind stress using 10-min-mean data collected from the same Saildrones. The agreement is best

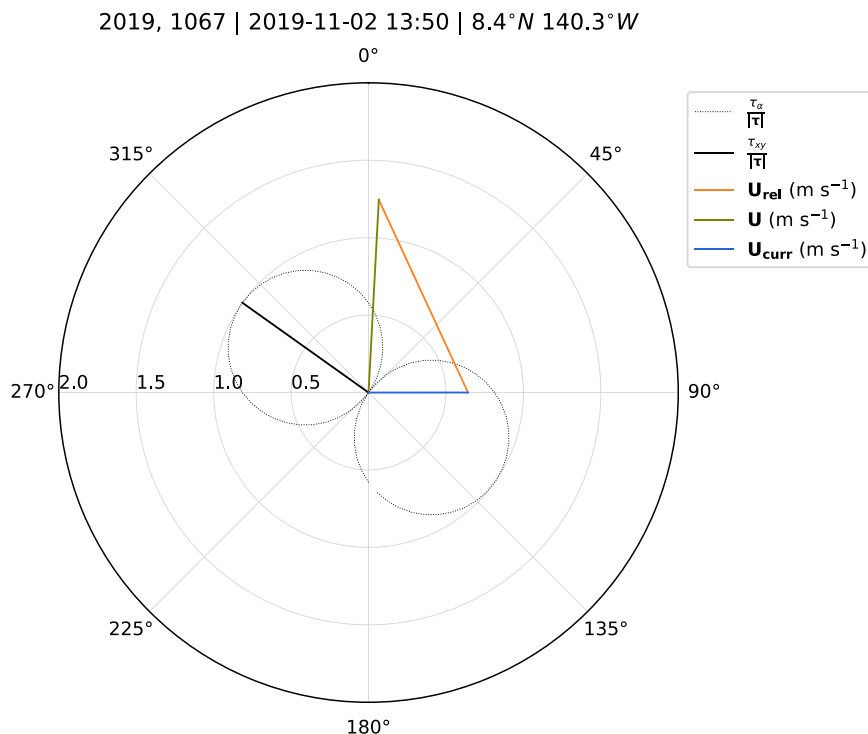


FIG. 9. Polar plot showing wind, current, and current-relative wind (units: m s^{-1}) and wind stress in relative units for the 10-min period beginning 1350 UTC 2 Nov 2019. The solid black line shows the direction of DC wind stress τ , scaled to length 1. The dashed black lines represent the magnitude (relative to $|\tau|$) of the streamwise component of DC wind stress when the calculation is performed in axes rotated to any direction. For example, the streamwise component of wind stress calculated in axes aligned with the wind direction (green line) would be slightly over half of $|\tau|$.

when only the streamwise component of DC wind stress, in the direction of the mean current-relative wind, is used. This is because the COARE 3.5 algorithm is based on such data. Even so, we think the cross-stream wind stress component contains meaningful signal, and we use it in other parts of this study.

The quality of the DC wind stress estimates supports several possible uses: 1) an alternative to bulk estimates when not all inputs are available for a bulk algorithm; 2) a complementary estimate when bulk data are available; 3) a source of data to better understand how currents, waves, and swell affect wind stress; 4) a possible source of data to improve bulk algorithms. The last of these uses would be greatly helped, however, by comparison with data from another proven DC measurement system.

Comparing drag coefficients calculated from DC wind stress with those from COARE 3.5 showed greatest differences for $|\mathbf{U}_{\text{rel}}| < 4 \text{ m s}^{-1}$. We quantified the contribution of wind stress direction assumptions to these low wind speed differences by examining the angles between DC wind stress and mean wind speed. For $|\mathbf{U}_{\text{rel}}| < 2 \text{ m s}^{-1}$, the wind direction and wind stress direction are essentially unrelated, while at higher wind speeds they align closely (within 22.5° in most cases). Recognizing that the current can have a significant effect on

wind stress at low wind speeds, we then explored whether Earth-relative or current-relative winds aligned more closely with wind stress direction. Looking at the set of cases where the current speed is at least half of the wind speed, the wind stress is significantly more closely aligned with the current-relative wind. This result demonstrates the impact of currents on wind stress direction, adding to findings in previous studies that currents are important for wind stress magnitude.

In the course of our research, we realized that the angle between the wind stress vector τ and current-relative wind \mathbf{U}_{rel} is related to the magnitude differences between the vector wind stress magnitude $|\tau|$ and the streamwise wind stress component $\tau_{x,\text{rel}}$. A two-dimensional rotation applied to the high-frequency wind data before the DC calculation is equivalent to the same rotation applied to the wind stress after the DC calculation. Effectively, $\tau_{x,\text{rel}}$ is the projection of τ onto \mathbf{U}_{rel} . This has important consequences for processing DC data and interpreting both DC and bulk wind stress estimates. We recommend that, unless the streamwise wind stress is explicitly needed (e.g., when tuning bulk flux algorithms), the vector wind stress should be used. This has a direction independent of the wind direction and a magnitude based on two perpendicular components (cross stream and streamwise, i.e., perpendicular and parallel to current-relative wind). Developers

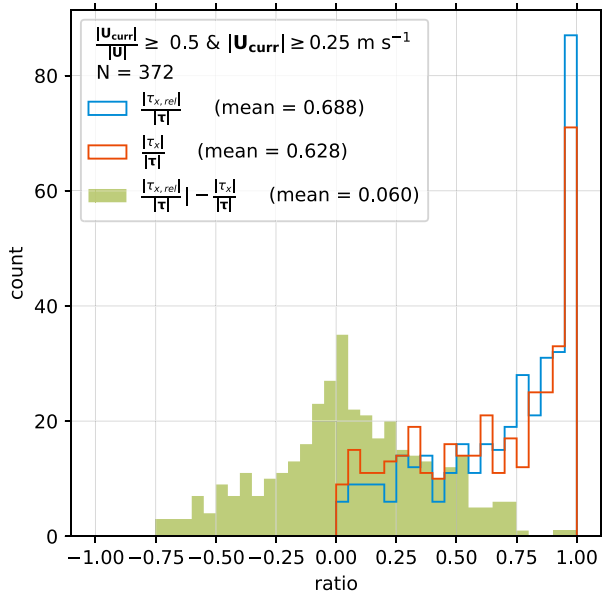


FIG. 10. Histogram of fractional differences between vector wind stress magnitude ($|\tau|$) and streamwise wind stress component for current-relative winds ($\tau_{x,rel}$, blue) and Earth-relative winds (τ_x , orange) for all 10-min periods (total: 372) where the current speed was at least half of the wind speed. The difference between the blue and orange curves is shown by the green shaded area. The values in parentheses in the legend are the means of the respective quantities.

and users of bulk flux algorithms should also be clear that bulk wind stress only represents the streamwise component of the true stress.

This investigation focused on the surface stress. Ongoing work is investigating the DC buoyancy flux (i.e., from the sonic temperature flux) compared to bulk values where we expect larger uncertainties in bulk heat flux estimates. It is worth noting that infrared hygrometers have been deployed on buoy-based systems to directly compute the latent heat flux (Clayson et al. 2019). This allows for removal of the moisture component in the sonic temperature flux to estimate the sensible heat flux. Given the good agreement between DC and bulk wind stress estimates in this study, the addition of an IR hygrometer on Saildrones should provide a means to improve latent and sensible heat flux parameterizations in bulk formulas.

Acknowledgments. We thank Saildrone, Inc., for their piloting and engineering efforts and for providing additional seadays during the 2017, 2018, and 2019 Saildrone missions. This work was partially funded by the Cooperative Institute for Climate, Ocean, and Ecosystem Studies (CIOCES) under NOAA Cooperative Agreement NA20OAR4320271, Contribution Number 2022-1199. This work was supported by NOAA's Global Ocean Monitoring and Observing Program, NOAA's Climate Program Office in the Climate Variability and Predictability Program as well as the Climate Observations and Monitoring Program, and NOAA's Office

of Marine and Aviation Operations. This is PMEL Contribution Number 5367.

Data availability statement. The raw Saildrone data (1 min and 10 Hz) are available from the NOAA Pacific Marine Environmental Laboratory (PMEL) ERDDAP (not an acronym) server at <https://data.pmel.noaa.gov/pmel/erddap/search/index.html?searchFor=TPOS>. The DC and bulk flux data used in this paper are available at <https://doi.org/10.5281/zenodo.6484830>. Software used to process the data and create the figures is available at <https://github.com/NOAA-PMEL/SaildroneCovarianceFlux/tree/v0.1.1> and <https://zenodo.org/record/7795063>. This repository also contains other utilities for handling high-frequency Saildrone data.

REFERENCES

- Bigorre, S. P., R. A. Weller, J. B. Edson, and J. D. Ware, 2013: A surface mooring for air–sea interaction research in the Gulf Stream. Part II: Analysis of the observations and their accuracies. *J. Atmos. Oceanic Technol.*, **30**, 450–469, <https://doi.org/10.1175/JTECH-D-12-00078.1>.
- Bourras, D., and Coauthors, 2019: Air-sea turbulent fluxes from a wave-following platform during six experiments at sea. *J. Geophys. Res. Oceans*, **124**, 4290–4321, <https://doi.org/10.1029/2018JC014803>.
- Chacko, N., M. M. Ali, and M. A. Bourassa, 2022: Impact of ocean currents on wind stress in the tropical Indian Ocean. *Remote Sens.*, **14**, 1547, <https://doi.org/10.3390/rs14071547>.
- Clayson, C. A., J. B. Edson, A. Paget, R. Graham, and B. Greenwood, 2019: Effects of rainfall on the atmosphere and the ocean during SPURS-2. *Oceanography*, **32** (2), 86–97, <https://doi.org/10.5670/oceanog.2019.216>.
- Cronin, M. F., C. W. Fairall, and M. J. McPhaden, 2006: An assessment of buoy-derived and numerical weather prediction surface heat fluxes in the tropical Pacific. *J. Geophys. Res.*, **111**, C06038, <https://doi.org/10.1029/2005JC003324>.
- , and Coauthors, 2019: Air-sea fluxes with a focus on heat and momentum. *Front. Mar. Sci.*, **6**, 430, <https://doi.org/10.3389/fmars.2019.00430>.
- Donelan, M. A., W. M. Drennan, and K. B. Katsaros, 1997: The air–sea momentum flux in conditions of wind sea and swell. *J. Phys. Oceanogr.*, **27**, 2087–2099, [https://doi.org/10.1175/1520-0485\(1997\)027<2087:TASMF1>2.0.CO;2](https://doi.org/10.1175/1520-0485(1997)027<2087:TASMF1>2.0.CO;2).
- Edson, J. B., and C. W. Fairall, 1998: Similarity relationships in the marine atmospheric surface layer for terms in the TKE and scalar variance budgets. *J. Atmos. Sci.*, **55**, 2311–2328, [https://doi.org/10.1175/1520-0469\(1998\)055<2311:SRITMA>2.0.CO;2](https://doi.org/10.1175/1520-0469(1998)055<2311:SRITMA>2.0.CO;2).
- , A. A. Hinton, K. E. Prada, J. E. Hare, and C. W. Fairall, 1998: Direct covariance flux estimates from mobile platforms at sea. *J. Atmos. Oceanic Technol.*, **15**, 547–562, [https://doi.org/10.1175/1520-0426\(1998\)015<0547:DCFEFM>2.0.CO;2](https://doi.org/10.1175/1520-0426(1998)015<0547:DCFEFM>2.0.CO;2).
- , and Coauthors, 2013: On the exchange of momentum over the open ocean. *J. Phys. Oceanogr.*, **43**, 1589–1610, <https://doi.org/10.1175/JPO-D-12-0173.1>.
- Fairall, C. W., J. B. Edson, S. E. Larsen, and P. G. Mestayer, 1990: Inertial-dissipation air–sea flux measurements: A prototype system using realtime spectral computations. *J. Atmos. Oceanic Technol.*, **7**, 425–453, [https://doi.org/10.1175/1520-0426\(1990\)007<0425:IDASFM>2.0.CO;2](https://doi.org/10.1175/1520-0426(1990)007<0425:IDASFM>2.0.CO;2).

- , E. F. Bradley, J. S. Godfrey, G. A. Wick, J. B. Edson, and G. S. Young, 1996a: Cool-skin and warm-layer effects on sea surface temperature. *J. Geophys. Res.*, **101**, 1295–1308, <https://doi.org/10.1029/95JC03190>.
- , —, D. P. Rogers, J. B. Edson, and G. S. Young, 1996b: Bulk parameterization of air-sea fluxes for tropical Ocean-Global Atmosphere Coupled-Ocean Atmosphere Response Experiment. *J. Geophys. Res.*, **101**, 3747–3764, <https://doi.org/10.1029/95JC03205>.
- , A. B. White, J. B. Edson, and J. E. Hare, 1997: Integrated shipboard measurements of the marine boundary layer. *J. Atmos. Oceanic Technol.*, **14**, 338–359, [https://doi.org/10.1175/1520-0426\(1997\)014<0338:ISMOTM>2.0.CO;2](https://doi.org/10.1175/1520-0426(1997)014<0338:ISMOTM>2.0.CO;2).
- , E. F. Bradley, J. E. Hare, A. A. Grachev, and J. B. Edson, 2003: Bulk parameterization of air-sea fluxes: Updates and verification for the COARE algorithm. *J. Climate*, **16**, 571–591, [https://doi.org/10.1175/1520-0442\(2003\)016<0571:BPOASF>2.0.CO;2](https://doi.org/10.1175/1520-0442(2003)016<0571:BPOASF>2.0.CO;2).
- Gaube, P., D. B. Chelton, R. M. Samelson, M. G. Schlax, and L. W. O'Neill, 2015: Satellite observations of mesoscale eddy-induced Ekman pumping. *J. Phys. Oceanogr.*, **45**, 104–132, <https://doi.org/10.1175/JPO-D-14-0032.1>.
- Geernaert, G. L., F. Hansen, M. Courtney, and T. Herbers, 1993: Directional attributes of the ocean surface wind stress vector. *J. Geophys. Res.*, **98**, 16571–16582, <https://doi.org/10.1029/93JC01439>.
- Grachev, A. A., C. W. Fairall, J. E. Hare, J. B. Edson, and S. D. Miller, 2003: Wind stress vector over ocean waves. *J. Phys. Oceanogr.*, **33**, 2408–2429, [https://doi.org/10.1175/1520-0485\(2003\)033<2408:WSVOOV>2.0.CO;2](https://doi.org/10.1175/1520-0485(2003)033<2408:WSVOOV>2.0.CO;2).
- Grare, L., L. Lenain, and W. K. Melville, 2018: Vertical profiles of the wave-induced airflow above ocean surface waves. *J. Phys. Oceanogr.*, **48**, 2901–2922, <https://doi.org/10.1175/JPO-D-18-0121.1>.
- Hanley, K. E., S. E. Belcher, and P. P. Sullivan, 2010: A global climatology of wind-wave interaction. *J. Phys. Oceanogr.*, **40**, 1263–1282, <https://doi.org/10.1175/2010JPO4377.1>.
- Högström, U., E. Sahlée, A.-S. Smedman, A. Rutgersson, E. Nilsson, K. K. Kahma, and W. M. Drennan, 2015: Surface stress over the ocean in swell-dominated conditions during moderate winds. *J. Atmos. Sci.*, **72**, 4777–4795, <https://doi.org/10.1175/JAS-D-15-0139.1>.
- Iyer, S., K. Drushka, E. J. Thompson, and J. Thomson, 2022: Small-scale spatial variations of air-sea heat, moisture, and buoyancy fluxes in the tropical trade winds. *J. Geophys. Res. Oceans*, **127**, e2022JC018972, <https://doi.org/10.1029/2022JC018972>.
- Janssen, P. A. E. M., 1999: On the effect of ocean waves on the kinetic energy balance and consequences for the inertial dissipation technique. *J. Phys. Oceanogr.*, **29**, 530–534, [https://doi.org/10.1175/1520-0485\(1999\)029<0530:OTEOW>2.0.CO;2](https://doi.org/10.1175/1520-0485(1999)029<0530:OTEOW>2.0.CO;2).
- Kelly, K. A., S. Dickinson, M. J. McPhaden, and G. C. Johnson, 2001: Ocean currents evident in satellite wind data. *Geophys. Res. Lett.*, **28**, 2469–2472, <https://doi.org/10.1029/2000GL012610>.
- Large, W. G., and S. Pond, 1981: Open ocean momentum flux measurements in moderate to strong winds. *J. Phys. Oceanogr.*, **11**, 324–336, [https://doi.org/10.1175/1520-0485\(1981\)011<0324:OOMFMI>2.0.CO;2](https://doi.org/10.1175/1520-0485(1981)011<0324:OOMFMI>2.0.CO;2).
- Mauder, M., M. Cuntz, C. Drüe, A. Graf, C. Rebmann, H. P. Schmid, M. Schmidt, and R. Steinbrecher, 2013: A strategy for quality and uncertainty assessment of long-term eddy-covariance measurements. *Agric. For. Meteorol.*, **169**, 122–135, <https://doi.org/10.1016/j.agrformet.2012.09.006>.
- Ortiz-Suslow, D. G., B. K. Haus, N. J. Williams, H. C. Graber, and J. H. MacMahan, 2018: Observations of air-sea momentum flux variability across the inner shelf. *J. Geophys. Res. Oceans*, **123**, 8970–8993, <https://doi.org/10.1029/2018JC014348>.
- , J. Kalogiros, R. Yamaguchi, and Q. Wang, 2021: An evaluation of the constant flux layer in the atmospheric flow above the wavy air-sea interface. *J. Geophys. Res. Atmos.*, **126**, e2020JD032834, <https://doi.org/10.1029/2020JD032834>.
- Prytherch, J., M. J. Yelland, I. M. Brooks, D. J. Tupman, R. W. Pascal, B. I. Moat, and S. J. Norris, 2015: Motion-correlated flow distortion and wave-induced biases in air-sea flux measurements from ships. *Atmos. Chem. Phys.*, **15**, 10619–10629, <https://doi.org/10.5194/acp-15-10619-2015>.
- Renault, L., M. J. Molemaker, J. C. McWilliams, A. F. Shchepetkin, F. Lemarié, D. Chelton, S. Illig, and A. Hall, 2016: Modulation of wind work by oceanic current interaction with the atmosphere. *J. Phys. Oceanogr.*, **46**, 1685–1704, <https://doi.org/10.1175/JPO-D-15-0232.1>.
- Soloviev, Y. P., and V. N. Kudryavtsev, 2010: Wind-speed undulations over swell: Field experiment and interpretation. *Bound.-Layer Meteorol.*, **136**, 341–363, <https://doi.org/10.1007/s10546-010-9506-z>.
- Starkenburg, D., S. Metzger, G. J. Fochesatto, J. G. Alfieri, R. Gens, A. Prakash, and J. Cristóbal, 2016: Assessment of despiking methods for turbulence data in micrometeorology. *J. Atmos. Oceanic Technol.*, **33**, 2001–2013, <https://doi.org/10.1175/JTECH-D-15-0154.1>.
- Sullivan, P. P., and J. C. McWilliams, 2010: Dynamics of winds and currents coupled to surface waves. *Annu. Rev. Fluid Mech.*, **42**, 19–42, <https://doi.org/10.1146/annurev-fluid-121108-145541>.
- Wills, S. M., M. F. Cronin, and D. Zhang, 2021: Cold pools observed by uncrewed surface vehicles in the central and eastern tropical Pacific. *Geophys. Res. Lett.*, **48**, e2021GL093373, <https://doi.org/10.1029/2021GL093373>.
- Zeng, X., M. Zhao, and R. E. Dickinson, 1998: Intercomparison of bulk aerodynamic algorithms for the computation of sea surface fluxes using TOGA COARE and TAO data. *J. Climate*, **11**, 2628–2644, [https://doi.org/10.1175/1520-0442\(1998\)011<2628:IOBAAF>2.0.CO;2](https://doi.org/10.1175/1520-0442(1998)011<2628:IOBAAF>2.0.CO;2).
- Zhang, D., and Coauthors, 2019: Comparing air-sea flux measurements from a new unmanned surface vehicle and proven platforms during the SPURS-2 field campaign. *Oceanography*, **32** (2), 122–133, <https://doi.org/10.5670/oceanog.2019.220>.